Journal of Materials Chemistry C

Accepted Manuscript

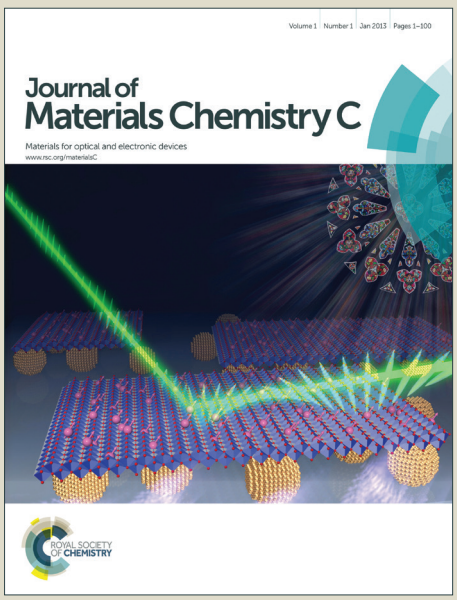

ROYAL SOCIETY OF CHEMISTRY

www.rsc.org/materialsC

ARTICLE TYPE
www. rsc.org/xxxxxx | XXXXXXXX

Absence of magnetic ordering in the ground state of a $SrTm_2O_4$ single crystal

Hai-Feng Li,*[a] Anatoliy Senyshyn,[b] Oscar Fabelo,[c] Jörg Persson,[d] Binyang Hou,[e] Martin Boehm,[c] Karin Schmalzl,[f] Wolfgang Schmidt,[f] Jean-Pierre Vassalli,[e] Pankaj Thakuria,[d] Xiao Sun,[d] Liming Wang,[d] Giorgi Khazaradze,[d] Berthold Schmitz,[d] Cong Zhang,[g] Georg Roth,[g] Javier García Roca [h] and Andrew Wildes *[c]

Received Xth XXXXXXXXXX 201X, Accepted Xth XXXXXXXXX 201X
First published on the web Xth XXXXXXXXXX 200X
DOI: 10.1039/b000000x

We report on the first single crystal study of $SrTm_2O_4$. Magnetization measurements along the crystallographic axes of a nearly stoichiometric $Sr_{1.07(3)}Tm_{2.07(6)}O_{4.00(2)}$ sample show either a positive or a negative Curie-Weiss temperature indicative of a competition between antiferromagnetic and ferromagnetic couplings. The field-dependent magnetization suggests an effective Zeeman splitting of the high-level *J*-multiplets above ∼8.3 T and that the paramagnetism may originate from only one of the two inequivalent Tm^{3+} crystallographic sites. Our single-crystal polarized neutron scattering and powder unpolarized neutron diffraction data show no evidence for either long- or short-range magnetic order even down to ∼65 mK. We reveal two TmO_6 octahedral distortion modes, i.e., one distortion is stronger than the other especially at low temperatures, which is attributed to different crystal fields of the two inequivalent octahedra. Therefore, the compound $SrTm_2O_4$ is unique and different from its brethren in the family of frustrated $SrRE_2O_4$ (*RE* = rare earth) magnets. We propose that crystal field anisotropy may dominate over weak dipolar spin interactions in $SrTm_2O_4$, thereby leading to a virtually non-ordered magnetic state.

1 Introduction

Geometric frustration, e.g., in edge-sharing tetrahedra, corner-shared networks in spinels or triangular Kagomé and pyrochlore lattices [1–5], often results in anomalous magnetic properties in lanthanide-based magnetic systems and prevents the relevant magnetic ions from ordering in the usual long-range fashion at low temperatures even far below the energy scale of individual spin-spin pair interactions. Consequently, structural distortion, short-ranged magnetic ordering and/or non-collinear magnetic structures may result to release or to indicate the frustration. This is accompanied normally by a reduction of the ordered moment from its theoretical saturation value [1–18].

The family of frustrated $SrRE_2O_4$ (*RE* = rare earth) compounds adopts an orthorhombic structure (space group $Pnam$) [19] which accommodates two inequivalent atomic sites for the RE ($RE1$ and $RE2$) ions. These compounds were first synthesized in 1967 [20]. A study of polycrystalline $SrRE_2O_4$ samples [21] reveals that the relevant RE ions are frustrated geometrically, where the short-range magnetic orders of $SrRE_2O_4$ (RE = Dy, Ho, Er) compounds persist down to ∼1.5 K; and no magnetic ordering was observed at ∼1.5 K in the $SrRE_2O_4$ (RE = Tm, Yb) compounds, which was attributed to the low magnetic moments of the heavy lanthanides Tm and Yb. One neutron scattering study of a $SrYb_2O_4$ single crystal reveals that the compound undergoes a magnetic phase transition upon cooling at T_N = 0.9, forming long-range commensurate noncollinear antiferromagnetic (AFM) order but with a reduction in the ordered moment compared to the ionic moment, i.e., the total ordered moments of the Yb1 (∼3.88 μ_B at 30 mK) and Yb2 (∼2.17 μ_B at 30 mK) sites are reduced from the theoretical full ionic value (4 μ_B) [22]. To our knowledge, no neutron scattering study of single-crystal $SrTm_2O_4$

[a] *Materials Science and Engineering and Chemical Engineering Department, Carlos III University of Madrid, Avda. de la Universidad 30, 28911 Leganés (Madrid), Spain. Tel: +34 6303035549123 (O); Fax: +34 916249430; E-mail: hfli@ing.uc3m.es*
[b] *Forschungsneutronenquelle Heinz Maier-Leibnitz FRM-II, Technische Universität München, Lichtenbergstrasse 1, D-85747 Garching bei München, Germany*
[c] *Institut Laue-Langevin, Boîte Postale 156, F-38042 Grenoble Cedex 9, France. E-mail: wildes@ill.fr*
[d] *Jülich Centre for Neutron Science JCNS and Peter Grünberg Institut PGI, JARA-FIT, Forschungszentrum Jülich GmbH, D-52425 Jülich, Germany*
[e] *European Synchrotron Radiation Facility, Boîte Postale 220, F-38043 Grenoble Cedex, France*
[f] *Jülich Centre for Neutron Science JCNS, Forschungszentrum Jülich GmbH, Outstation at Institut Laue-Langevin, Boîte Postale 156, F-38042 Grenoble Cedex 9, France*
[g] *Institut für Kristallographie der RWTH Aachen University, D-52056 Aachen, Germany*
[h] *Departamento de Química Inorgánica I, Facultad de Ciencias Químicas, Universidad Complutense, 28040 Madrid, Spain*

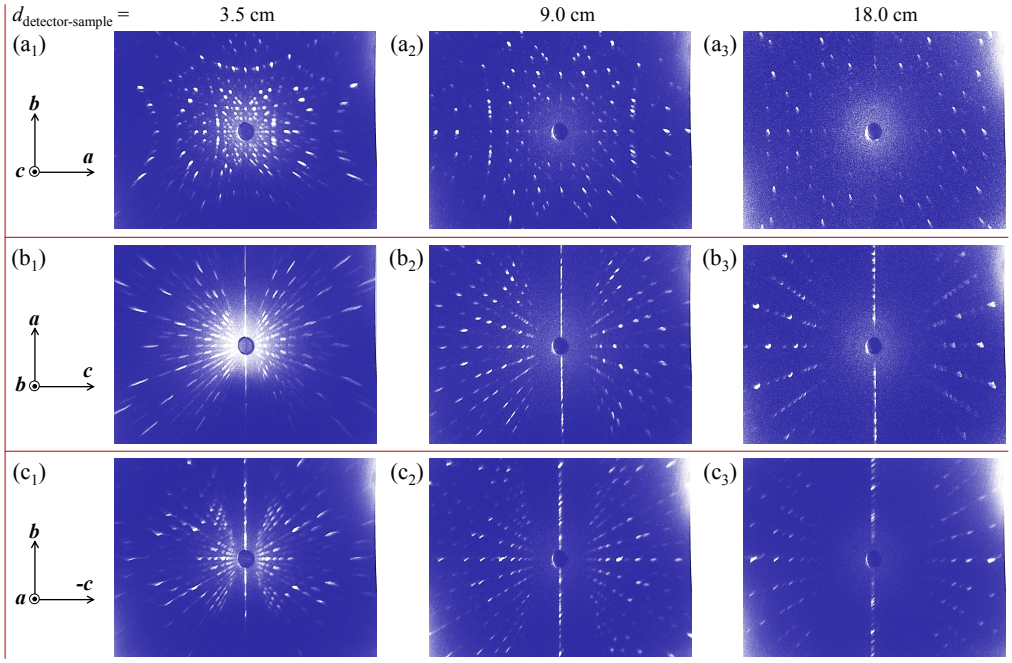

Fig. 1 Complete neutron Laue patterns of single-crystal $SrTm_2O_4$ with real-space lattice vectors as displayed, which was measured with the neutron Laue diffractometer, OrientExpress[23], located at ILL. The distances between a detector and the sample are 3.5 cm (a_1, b_1, c_1), 9.0 cm (a_2, b_2, c_2), and 18.0 cm (a_3, b_3, c_3), respectively. We chose a pinhole with 3 mm diameter for the neutron beam impinging on the crystal and a 20-mins exposure. The incoming neutron beam is perpendicular to the planes of the Laue spots and thus parallel to the unit-cell edges, i.e., the neutron beam was running along the *c* axis (a_1, a_2, a_3), *b* axis (b_1, b_2, b_3), and *a* axis (c_1, c_2, c_3), respectively.

has been reported[16]. Recently, the magnetic ordering of another frustrated candidate $BaNd_2O_4$ with the same isostructural symmetry as that of the $SrRE_2O_4$ family has been reported[24]. Besides scientific research interests, the Eu lightly-doped SrY_2O_4 compound promises a potential application to temperature sensors[25].

To shed light on the nature of the magnetic frustration in $SrRE_2O_4$ compounds, it is crucial to explore the spin states and related frustrations in all $SrRE_2O_4$ compounds. In this paper, we report on the first single crystal study of the compound $SrTm_2O_4$. Surprisingly, both polarized and unpolarized neutron scattering studies show no sign of any types of magnetic order down to ~65 mK. These observations render $SrTm_2O_4$ a unique compound in the family for theoretical and further experimental explorations.

2 Experimental

Polycrystalline and single-crystalline samples of the compound $SrTm_2O_4$ were synthesized with the similar procedures to those reported previously[26–29]. The chemical stoichiometry of the single crystal being studied here was quantitatively estimated by inductively coupled plasma with optical emission spectroscopy (ICP-OES) analysis. The dc magnetization of a $SrTm_2O_4$ single crystal with orientated crystallographic directions was measured as a function of temperature from ~1.9-300 K at 1 T using a Quantum Design MPMS-7 SC quan-

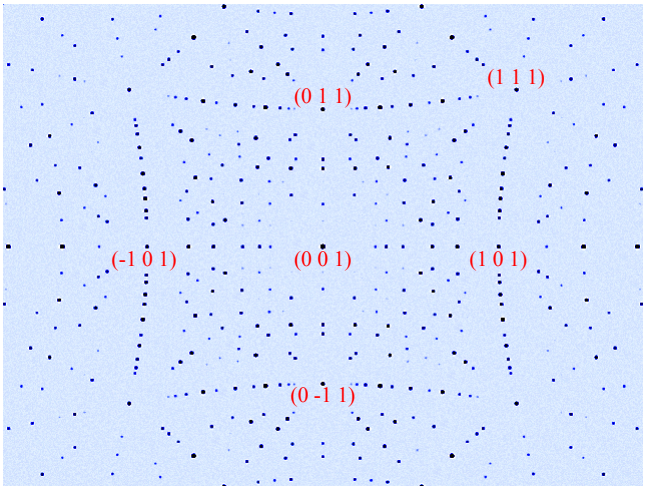

Fig. 2 An accurate simulation of Fig. 1(a_2) by the software Esmeralda Laue Suite[30] with the same experimental parameters. The index of some selected reflections have been highlighted in order to clearly identify the crystallographic axes.

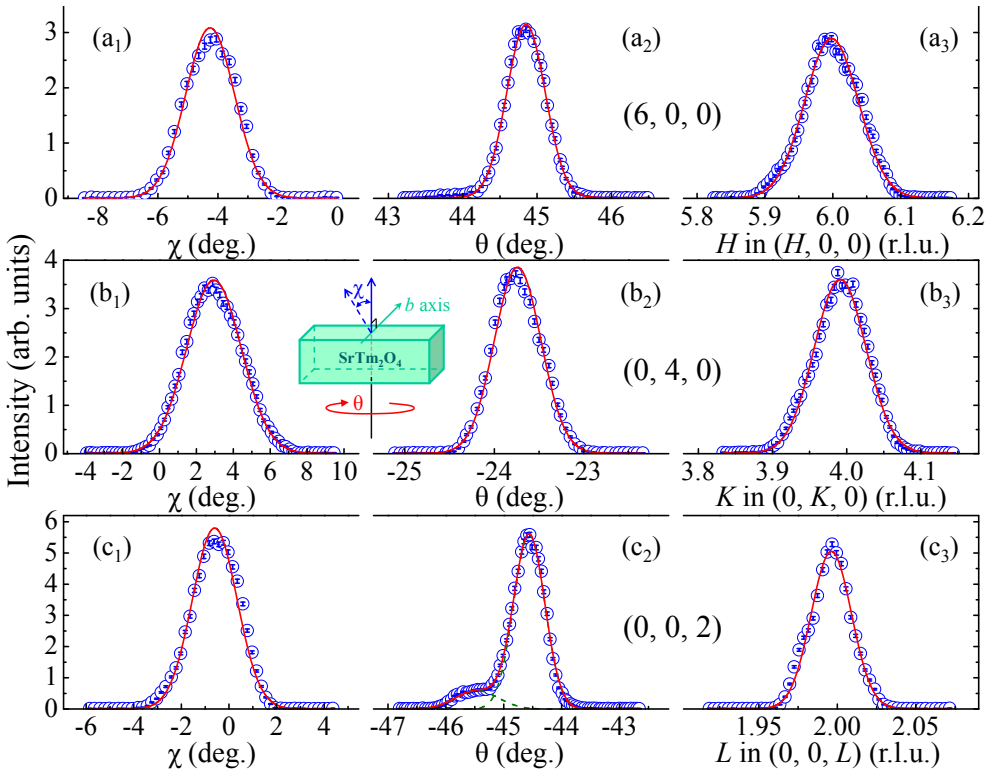

Fig. 3 Neutron diffraction data (circles) of the Bragg (6, 0, 0) (a_1, a_2, a_3), (0, 4, 0) (b_1, b_2, b_3) and (0, 0, 2) (c_1, c_2, c_3) nuclear reflections measured at room temperature using IN3 (ILL). (a_1, b_1, c_1) The corresponding χ scans show the misorientation of the single crystal. (a_2, b_2, c_2) The corresponding rocking curve θ-scans indicate the mosaic spread of the single crystal. (a_3, b_3, c_3) The corresponding **Q**-scans along the H, K and L directions in reciprocal space. The lines are Gaussian fits. Inset schematically shows the angles χ (denoting a rotation out of the scattering plane) and θ (denoting a rotation within the scattering plane) in real space for the corresponding scans around the b axis.

tum interference device (SQUID) magnetometer. The high-temperature (∼580-880 K) dc magnetization at 1.5 T of another $SrTm_2O_4$ sample with unknown crystallographic orientations and the dc magnetization of powdered $SrTm_2O_4$ samples as a function of applied magnetic field (up to 9 T) at 2 K, 40 K and 80 K were measured using a commercial physical property measurement system (PPMS). The field-dependent magnetization was acquired after cooling in zero magnetic field (ZFC).

We cleaved a piece of the $SrTm_2O_4$ single crystal with a mass of ∼0.8 g for the following neutron-scattering studies. This sample was oriented in the $(H, K, 0)$ scattering plane of the orthorhombic symmetry with the neutron Laue backscattering diffractometer, OrientExpress[23], at the Institut Laue-Langevin (ILL), Grenoble, France. Neutron diffraction study was performed at room temperature using the IN3 (ILL) thermal triple-axis spectrometer with fixed final energy at ∼14.67 meV. Uniaxial longitudinal neutron polarization analysis was carried out on the D7 (ILL) diffractometer[31] at a wavelength $\lambda = 4.8$ Å equipped with a dilution refrigerator. The scattering from an amorphous quartz standard was used to calibrate the polarization efficiency for each detector, giving a mean polarization of ∼0.88. The data were calibrated with vanadium for detector efficiency and with amorphous quartz for polarization corrections. The corresponding background was measured at ∼1.6 K using an empty sample holder. Measurements were carried out with the neutron polarization, $\hat{\mathbf{P}}$, aligned normal to the scattering plane (defined as the Z-direction).

High-resolution neutron powder diffraction (NPD) patterns were collected at temperatures 0.5 K and 4 K on the structure powder diffractometer (SPODI)[32] at the FRM-II research reactor in Garching, Germany. The wavelength was fixed at λ = 2.54008(2) Å which has been obtained from the refinement of Si standard. The rest of the $SrTm_2O_4$ single crystal (∼3.91 g) was gently ground into powder and then sealed in a cylindrical vanadium container that was mounted in a ^{3}He insert with a normal cryorefrigerator. The detector was scanned with a typical step size of 0.05°. The NPD data were refined with the Fullprof suite[33]. A Pseudo-Voigt function was used to model the peak profile shape. The background was refined using a linear interpolation between selected data points. The scale factor, zero shift, wavelength, peak shape parameters, asym-

metry, lattice parameters, atomic positions, isotropic thermal parameter B as well as the preferred orientation (from a powder diffraction), etc., were all refined with some constrains.

Throughout this paper, the wave vector $\mathbf{Q}_{(H,K,L)}$ (Å^{-1}) = ($\mathbf{Q}_H$, $\mathbf{Q}_K$, $\mathbf{Q}_L$) is defined through (H, K, L) = ($\frac{a}{2\pi}Q_H$, $\frac{b}{2\pi}Q_K$, $\frac{c}{2\pi}Q_L$) quoted in units of r.l.u., where a, b, and c are relevant lattice parameters referring to the orthorhombic unit cell.

3 Results

3.1 ICP-OES measurements

From our ICP-OES measurements, we determine the mole chemical compositions as $Sr_{1.07(3)}Tm_{2.07(6)}O_{4.00(2)}$, indicating that the single crystal being studied here is nearly stoichiometric within the experimental accuracy.

3.2 Neutron Laue diffraction patterns

To precisely determine the crystallographic orientations for the following neutron diffraction studies and magnetization measurements along the a, b and c axes, we record the regularly-spaced Bragg diffraction spots of $SrTm_2O_4$ with a neutron Laue diffractometer equipped with a CCD detector coupled to a neutron scintillator. The complete back-diffraction patterns mapping the [u, v, 0] (Fig. 1(a)), [u, 0, w] (Fig. 1(b)) and [0, v, w] (Fig. 1(c)) zone indices are displayed in Fig. 1. When the distance between a detector and the examined single crystal $d_{\mathtt{detector-sample}} \sim 3.5$ cm (Figs. 1(a_1), 1(b_1), 1(c_1)), it is easy to distinguish the c axis from the a and b axes (Figs. 1(b_1), 1(c_1)) due to the big difference between the c lattice constant and the a and b lattice constants (Table 1). However, it is not easy to clearly distinguish the a from the b axis due to the proximity of the lattice constants a and b (Table 1), though the Laue patterns (Figs. 1(a_1), 1(b_1), 1(c_1)) are highly symmetrical (practically, 2-fold) with sets of Laue spots arranged in rings or lines about the center of the respective patterns. The separation of the Bragg reflections was done by increasing the detector-sample distances to ~9 cm (Figs. 1(a_2), 1(b_2), 1(c_2)) and ~18 cm (Figs. 1(a_3), 1(b_3), 1(c_3)). These images were oriented using the OrientExpress software[23]. A confirmation of the obtained orientations was done by simulations of the Laue patterns of $SrTm_2O_4$ compound using the Esmeralda Laue Suite[30]. The Laue patterns together with the determination of the crystallographic directions are shown in Fig. 1. One representative simulation of Fig. 1(a_2) in addition to associated indices is schematically shown in Fig. 2. We thus can assign the Laue spots to detailed crystal planes that reflect off the incoming neutron beam and generate them and determine the crystallographic directions.

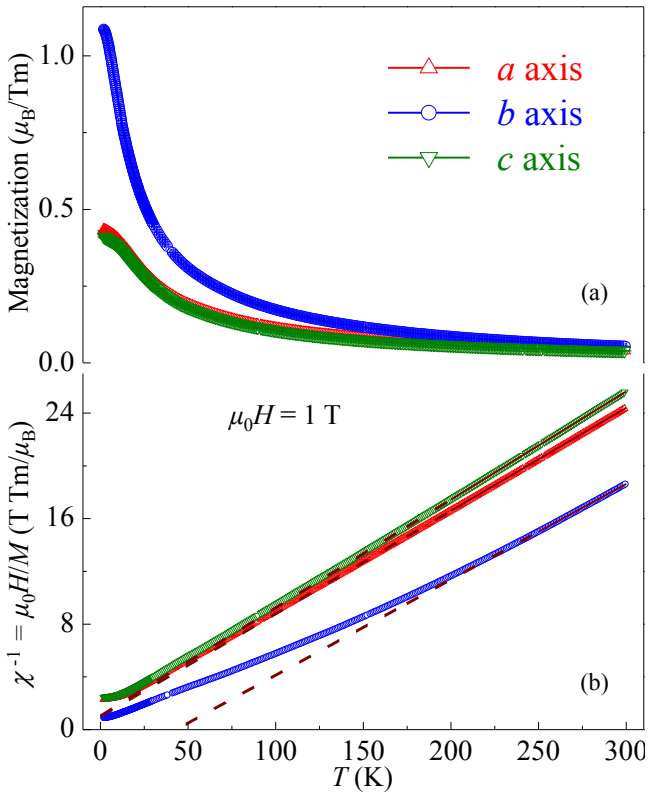

Fig. 4 (a) ZFC Magnetization normalized to a single Tm^{3+} ion along the crystallographic a, b and c axes as a function of temperature from ~1.9 to 300 K at 1 T. Due to a high density of data points (~440 at each axis), they almost overlap each other. (b) The corresponding inverse magnetic susceptibility χ^{-1} (symbols) deduced from the magnetization measurements as shown in (a). The solid lines are fits to the data (along the a axis: 200-300 K, 109 points; along the b axis: 250-300 K, 56 points; along the c axis: 200-300 K, 109 points) with a Curie-Weiss law (eqn (1)) as described in the text and extrapolated to lower temperatures (dashed lines). The fit results are listed in Table 2.

3.3 Neutron diffraction study

We characterized the single crystal by a neutron diffraction study at room temperature as shown in Fig. 3. The angle χ (Fig. 3) in the IN3 scattering geometry represent the size of misorientation of the single crystal. By fitting the data (circles in Figs. 3(a_1), 3(b_1), 3(c_1)) to a Gaussian function, we find that the misorientations of the a, b and c axes are ~4.3° (Fig. 3(a_1)), ~3.0° (Fig. 3(b_1)) and ~0.6° (Fig. 3(c_1)), respectively, which was probably resulting from a re-mounting of the sample. The full width at half maximum for the nuclear Bragg (6, 0, 0), (0, 4, 0) and (0, 0, 2) reflections are 0.61(1)°, 0.61(1)° and 0.63(1)°, respectively, indicating an almost isotropic mosaic spread in real space within the present experimental accuracy. The **Q**-scans along the H (Fig. 3(a_3)), K (Fig. 3(b_3))

Table 1 Refined structural parameters (lattice constants *a*, *b* and *c*, atomic positions, Debye-Waller thermal parameter *B*) and associated bond angles and bond lengths as well as the corresponding goodness of refinements by the Fullprof Suite[33] from the NPD data measured at 0.5 K and 4 K using SPODI (FRM-II). We list the lengths of NNB, NNNB and the next-NNN (NNNNB) Tm1-Tm1, Tm2-Tm2 and Tm1-Tm2 bonds for discussion in the text. The calculated unit-cell volume *V*, average bond-lengths ⟨Tm1-O1,2,3⟩ and ⟨Tm2-O1,3,4⟩, and the extracted octahedral distortion parameter Δ (as defined in the text) are also listed. All atoms are located at the Wyckoff site 4c, i.e., (*x*, *y*, 0.25). Number in parenthesis is the estimated standard deviation of the last or the next last significant digit.

Pulverized single-crystal $SrTm_2O_4$ (Orthorhombic, space group: *Pnam*)						
T (K)		0.5			4	
a, b, c (Å)	9.9759(1)	11.8150(1)	3.3809(1)	9.9764(1)	11.8148(1)	3.3811(1)
α, β, γ (°)	90	90	90	90	90	90
V (Å^3)		398.490(6)			398.523(6)	
Atom	x	y	B (Å^2)	x	y	B (Å^2)
Sr	0.7536(2)	0.6501(2)	0.65(8)	0.7529(3)	0.6489(3)	0.54(8)
Tm1	0.4218(3)	0.1084(3)	0.52(7)	0.4210(3)	0.1075(3)	0.33(7)
Tm2	0.4244(3)	0.6133(2)	0.14(7)	0.4238(3)	0.6125(3)	0.64(8)
O1	0.2104(3)	0.1723(2)	0.40(9)	0.2103(3)	0.1739(3)	0.53(9)
O2	0.1236(2)	0.4807(2)	0.70(9)	0.1256(3)	0.4806(3)	0.40(10)
O3	0.5160(3)	0.7840(2)	0.32(8)	0.5154(3)	0.7832(2)	0.52(9)
O4	0.4250(3)	0.4239(2)	0.56(9)	0.4259(3)	0.4247(2)	0.26(10)
∠Tm1-O2-Tm1 (°)	94.04(10), 97.41(20)			94.24(12), 96.6(2)		
∠Tm1-O3-Tm1 (°)	100.15(10)			99.20(10)		
∠Tm1-O1-Tm2 (°)	117.0(2)			116.1(2)		
∠Tm1-O3-Tm2 (°)	129.9(2)			130.4(2)		
∠Tm2-O1-Tm2 (°)	96.28(10)			96.01(11)		
∠Tm2-O4-Tm2 (°)	94.40(10), 101.10(16)			94.51(10), 101.4(2)		
∠O1-Tm1-O2 (°)	172.1(2), 92.04(17)			173.4(3), 92.2(2)		
∠O2-Tm1-O3 (°)	173.13(15), 91.02(16)			173.57(18), 90.55(18)		
∠O3-Tm2-O4 (°)	155.5(2), 84.53(15)			155.1(2), 84.55(16)		
∠O1-Tm2-O4 (°)	172.48(17), 107.98(17)			171.80(18), 108.9(2)		
Tm1-Tm1 (NNB, NNNB, NNNNB) (Å)	3.3809, 3.4428, 5.8918			3.3810, 3.4344, 5.8871		
Tm2-Tm2 (NNB, NNNB, NNNNB) (Å)	3.3809, 3.5072, 5.9297			3.3810, 3.4980, 5.9245		
Tm1-Tm2 (NNB, NNNB, NNNNB) (Å)	3.8456, 4.0029, 5.6110			3.8333, 4.0248, 5.6000		
Tm1-O1 (× 1) (Å)	2.2400(42)			2.2437(43)		
Tm1-O2 (× 3) (Å)	2.2718(37), 2.3107(29) (× 2)			2.2913(44), 2.3069(34) (× 2)		
Tm1-O3 (× 2) (Å)	2.2043(27)			2.2199(28)		
Tm2-O1 (× 2) (Å)	2.2698(27)			2.2746(30)		
Tm2-O3 (× 1) (Å)	2.2142(35)			2.2142(43)		
Tm2-O4 (× 3) (Å)	2.2378(33), 2.3039(28) (× 2)			2.2189(43), 2.3020(29) (× 2)		
⟨Tm1-O1,2,3⟩ (Å)	2.2569(13)			2.2648(15)		
⟨Tm2-O1,3,4⟩ (Å)	2.2665(12)			2.2644(14)		
Δ (×10^{-4})	Tm1: 3.870, Tm2: 2.069			Tm1: 2.836, Tm2: 2.482		
$R_p, R_{wp}, R_{exp}, \chi^2$	2.07, 2.73, 1.14, 5.76			2.39, 3.24, 1.58, 4.19		

and *L* (Fig. 3(c$_3$)) directions confirm the former determination of the crystallographic directions by neutron Laue backscattering.

3.4 Magnetization *versus* temperature

We first measured the dc magnetization of $SrTm_2O_4$ along its crystallographic *a*, *b* and *c* axes as shown in Fig. 4. Fig. 4(a) shows that with decreasing temperature the magnetization along the *b* axis increases in the whole temperature range and is clearly higher than those along the *a* and *c* axes; by comparison, below ∼10 K, the increases of the magnetization along the *a* and *c* axis become relatively slow so that there are clear kinks in the data curves around 10 K.

The linear increase of the inverse magnetic susceptibility $\chi^{-1} = \mu_0 H/M$ with temperature in a paramagnetic (PM) state obeys well the molar susceptibility according to the Curie-Weiss (CW) law:

$$\chi(T) = \frac{C}{T - \theta_{\rm CW}} = \frac{N_A M_{\rm eff}^2}{3k_B(T - \theta_{\rm CW})}, \quad (1)$$

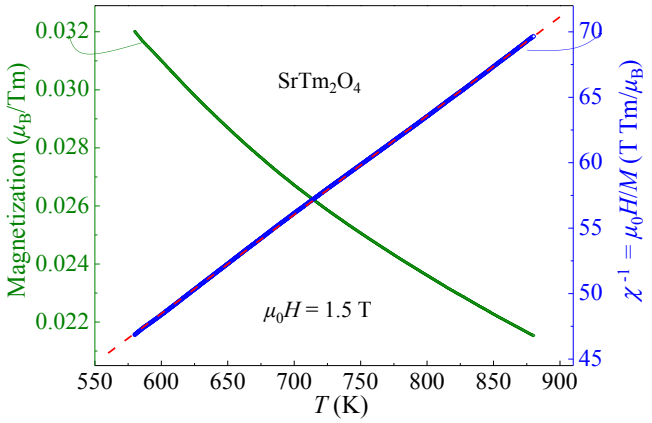

Fig. 5 Magnetization normalized to a single Tm^{3+} ion as a function of temperature from ~580 to 880 K at 1.5 T (left ordinate) and the corresponding inverse magnetic susceptibility χ^{-1} (right ordinate). The dashed line is a fit to the data with a Curie-Weiss law (eqn (1)).

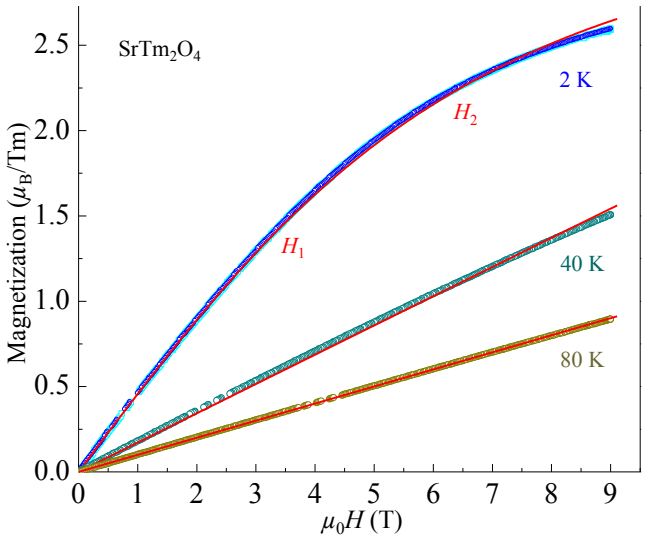

Fig. 6 As displayed, ZFC magnetization measurements at 2 K with a loop of increasing (0 to 9 T) and decreasing (9 to 0 T) magnetic field (circles, both field-dependent curves overlap each other due to a high-density of data points and thus are indistinguishable) and ZFC magnetization as a function of applied magnetic field at 40 K and 80 K (circles). It is clear that no appreciable hysteresis effect appears in single-crystal $SrTm_2O_4$ at 2 K as observed in traditional ferromagnets. The solid lines are fits to the eqn (2) (details in the text). H_1 and H_2 are marked for discussion in the text.

where C is the Curie constant, $\theta_{\rm CW}$ is the CW temperature, N_A = 6.022 × 10^{23} mol^{-1} is the Avogadro's number, $M_{\rm eff}$ is the effective PM moment, and k_B = 1.38062 × 10^{-23} J/K is the Boltzmann constant. Fig. 4(b) shows our fits (solid lines) to the data with eqn (1) in the respective temperature regimes, and the derived results are listed in Table 2.

To extract the intrinsic PM properties of $SrTm_2O_4$, we measured the high-temperature (~580-880 K) magnetization at 1.5 T as shown in Fig. 5. From the fit to the data with eqn (1), shown as the dashed line in Fig. 5, we derive a measured $M^{\rm eff}_{\rm mea}$ = 7.69(1) $\mu_{\rm B}$ per Tm^{3+} ion. This value is very close to the expected theoretical value $M^{\rm eff}_{\rm theo}$ ~ 7.56 $\mu_{\rm B}$ of the ground state $^3H_6$ determined by the Hund's rules. This is consistent with the fact that the studied single crystal is almost stoichiometric. We also deduce that $\theta_{\rm CW}$ = -41.6(2) K, implying a net AFM coupling strength.

3.5 Magnetization *versus* magnetic field

To explore the Tm^{3+} magnetic state and possible high magnetic-field effect on the high-level J-multiplets using eqn (2) as discussed below, we measured the field-dependent magnetization of powdered $SrTm_2O_4$ samples as shown in Fig. 6. The measured moment size per Tm^{3+} ion at 9 T and 2 K is 2.60(1) $\mu_{\rm B}$, ~37.1% of the corresponding theoretical value 7.0 $\mu_{\rm B}$, indicative of a strong single-ion anisotropy due to crystal field effects[34]. The nonlinear field-dependence at low temperatures as shown in Fig. 6 would result from pure paramagnetism, ferromagnetism, a magnetic-polaron state[35] or a short-range AFM state taking into account the processes of spin-flop and spin-flip transitions with increasing field[34,36,37]. At 2 K, there is no appreciable magnetic hysteresis effect detected. This, along with the fact that the studied single crystal is nearly stoichiometric, clearly rules out the possibility for a ferromagnet. The field-dependent magnetization at low temperatures obeys a Brillouin function modified specifically for a frustrated paramagnet:

$$M(H) = \eta M^{\rm sat}_{\rm theo} B_J(x), \text{with}$$
$$B_J(x) = \frac{2J+1}{2J} coth(\frac{2J+1}{2J}x) - \frac{1}{2J} coth(\frac{1}{2J}x), \quad (2)$$

where η denotes the degree of the magnetic frustration, $M^{\rm sat}_{\rm theo}$ is the theoretical value of the saturation mole moment, J is the total angular momentum, and $x = \frac{g_J J \mu_B H}{k_B T}$. The corresponding values of these parameters are listed in Table 2. Eqn (2) was used to fit the measured data as shown in Fig. 6, giving $\eta = 0.504(1)$ at 2 K.

3.6 Polarization analysis at D7

Figure 7 shows neutron polarization analysis data in the spin flip (SF, i.e., flipper on) and non-spin flip (NSF, i.e., flipper off) channels. Polarized neutron magnetic scattering depends on the direction of the neutron polarization $\hat{\mathbf{P}}$ with respect to the scattering vector $\hat{\mathbf{Q}}$ and also the direction of the ordered-moments $\hat{\boldsymbol{\mu}}$. In our study, $\hat{\mathbf{P}}$ is normal to the scattering plane and also parallel to the c axis[31]. In this configuration, taking into account the fact that the compound $SrTm_2O_4$ does

Table 2 The quantum numbers of single-crystal $SrTm_2O_4$: spin S, orbital L, total angular momentum J as well as Landé factor g_J and ground-state term $^{2S+1}L_J$. We also summarize the theoretical (theo) and measured (mea) values of the effective (eff) and saturation (sat) Tm^{3+} moments, μ_{eff} and μ_{sat}, respectively, the CW temperature, θ_{CW}, and the frustrating parameter η included in eqn 2. Number in parenthesis is the estimated standard deviation of the last significant digit.

$SrTm_2O_4$ single crystal	
$4f$ ion	Tm^{3+}
$4f^n$	12
S	1
L	5
$J = L + S$ (Hund's rule for free Tm^{3+})	6
g_J	7/6
$^{2S+1}L_J$	$^3H_6$
$M^{\mathrm{eff}}_{\mathrm{theo}} = g_J\sqrt{J(J+1)}$ (μ_B)	~7.56
$M^{\mathrm{sat}}_{\mathrm{theo}} = g_J J$ (μ_B)	7.00
$M^{\mathrm{eff}}_{\mathrm{mea}}/Tm^{3+}$ (*a* axis, 200-300 K, 1 T) (μ_B)	7.56(1)
$M^{\mathrm{eff}}_{\mathrm{mea}}/Tm^{3+}$ (*b* axis, 250-300 K, 1 T) (μ_B)	7.85(1)
$M^{\mathrm{eff}}_{\mathrm{mea}}/Tm^{3+}$ (*c* axis, 200-300 K, 1 T) (μ_B)	7.38(1)
$M^{\mathrm{eff}}_{\mathrm{mea}}/Tm^{3+}$ (580-880 K, 1.5 T) (μ_B)	7.69(1)
θ_{CW} (*a* axis, 200-300 K, 1 T) (K)	-12.7(1)
θ_{CW} (*b* axis, 250-300 K, 1 T) (K)	43.0(2)
θ_{CW} (*c* axis, 200-300 K, 1 T) (K)	-12.7(1)
θ_{CW} (580-880 K, 1.5 T) (K)	-41.6(2)
M_{mea}/Tm^{3+} (2 K, 9 T) (μ_B)	2.60(1)
η (eqn 2)	0.504(1)

not display any ferrimagnetic component, the spin-dependent cross-sections may be written as:

$$(\frac{d\sigma}{d\Omega})^{\mathrm{SF}} = \frac{2}{3}(\frac{d\sigma}{d\Omega})_{\mathrm{nsi}} + (\frac{d\sigma}{d\Omega})^{\perp}_{\mathrm{mag}} \text{ and} \quad (3)$$

$$(\frac{d\sigma}{d\Omega})^{\mathrm{NSF}} = \frac{1}{3}(\frac{d\sigma}{d\Omega})_{\mathrm{nsi}} + (\frac{d\sigma}{d\Omega})_{\mathrm{nuc}} + (\frac{d\sigma}{d\Omega})^{\parallel}_{\mathrm{mag}}, \quad (4)$$

where

$$(\frac{d\sigma}{d\Omega})_{\mathrm{mag}} = \frac{2}{3}(\frac{\gamma_n r_e}{2})^2 f^2_M(|\mathbf{Q}|) g^2_J J(J+1), \quad (5)$$

where γ_n = -1.913 is the neutron gyromagnetic ratio, $r_e = 2.81794 \times 10^{-5}$ Å is the classical electron radius, $f_M(|\mathbf{Q}|)$ is the magnetic form factor at the magnetic reciprocal lattice ($\mathbf{Q}$), g_J and J are the Landé factor and total angular momentum, respectively. The cross-section subscript *nsi* refers to the nuclear spin incoherent contribution. The subscript *nuc* refers to nuclear and isotopic incoherent contributions. The magnetic contributions, given by the subscript *mag*, are subdivided into two parts: those components that are perpendicular to both $\hat{\mathbf{P}}$ and $\hat{\mathbf{Q}}$ give rise to SF scattering[31], i.e.,

$$(\frac{d\sigma}{d\Omega})^{\perp}_{\mathrm{mag}} \propto \langle \hat{\mu} \parallel (\hat{\mathbf{P}} \times \hat{\mathbf{Q}}) \rangle^2; \quad (6)$$

those components of $\hat{\boldsymbol{\mu}}$ that are parallel to $\hat{\mathbf{P}}$, hence normal to the scattering plane and parallel to the *c* axis, give rise to NSF scattering, i.e.,

$$(\frac{d\sigma}{d\Omega})^{\parallel}_{\mathrm{mag}} \propto \langle \hat{\mu} \parallel \hat{\mathbf{P}} \rangle^2. \quad (7)$$

Figure 7 displays no obvious magnetic scattering at ~65 mK from either long- or short-ranged magnetic ordering. The NSF scattering displayed in Fig. 7(a) shows Bragg peaks that can be indexed with the corresponding orthorhombic structure. There is some parasitic intensity visible in the SF scattering as shown in Fig. 7(b) due to small errors coming from the imperfect polarization correction. However, there are indeed no new Bragg peaks, which would imply a long-range magnetic order with the nonzero propagation vector, nor is there any obvious diffuse scattering from short-ranged ordering, within the $(H, K, 0)$ scattering plane.

3.7 NPD study at SPODI

We performed a NPD analysis as shown in Fig. 8. The large mass of the measured powder and the considerable counting time (e.g., ~26 h at 0.5 K) enabled us to detect possible magnetic neutron scattering signal as verified in the studies of references 40 and 43 where the same neutron diffractometer SPODI was used. The Bragg peaks in the collected NPD patterns can be indexed by the orthorhombic structural model, which rules out possible magnetic ordering with a nonzero propagation wave vector consistent with our polarization analysis presented above.

Figure 9 schematically depicts the resulting crystal structure (Fig. 9(a)), local connections of the TmO_6 octahedra (Figs. 9(b), 9(c)), as well as the bent Tm_6 honeycomb and its projection to the *ab* plane (Figs. 9(d) and 9(e), respectively). The TmO_6 octahedra build up a 3D network in the way of sharing edges between $Tm1O_6$ or $Tm2O_6$. The connections between both types of octahedra are their in-plane and spatial corners. By way of example, two nearest $Tm1O_6$ octahedra (Fig. 9(b)) share a common O2-O3 bond along the *c* axis, and the Tm1 and Tm2 sites are connected by the O1 or O3 ions (Fig. 9(a)).

Based on the irreducible representation analysis to the lower *P*-1 symmetry[33], we tried all possible magnetic models with a propagation wave vector at $\mathbf{Q}$ = (0, 0, 0)[22] to analyze the NPD data. One representative Fullprof[33] refinement is displayed in Fig. 10. We find a reasonable refinement only when the Tm moments are along the *c* axis in agreement with our magnetization measurements as shown in Fig. 4, although the values of the goodness-of-fit give no appreciable improvement in comparison with those from the refinement with only nuclear structural model (Table 1). The resulting Tm1 and Tm2 moments are +0.30(21) and -0.20(21) μ_B at 0.5 K, respectively.

This suggests that there is no ordered moment and thus no long-ranged magnetic ordering at all consistent with our magnetic characterizations. We, therefore, conclude that $SrTm_2O_4$ is a totally-frustrated compound at least at $T \geq 65$ mK.

4 Discussion

As listed in Table 2, it is noteworthy that the derived effective PM moments are ∼7.56 μ_B, ∼7.85 μ_B, and ∼7.38 μ_B, and the CW temperatures are ∼-12.7 K, ∼43.0 K, and ∼-12.7 K along the *a*, *b*, and *c* axes, respectively, indicating a strong competition between AFM and ferromagnetic couplings that may result in the magnetic frustrations in $SrTm_2O_4$. The effective PM moment along the *b* axis is higher than the expected theoretical value (Table 2), implying that magnetic polarons[35,38–42] may form in that direction consistent with the fact that its derived CW temperature is positive. The upward deviations of the inverse magnetic susceptibility χ^{-1} from our calculations based on the theoretical CW law (Fig. 4(b)), especially along the *b* axis, indicate that AFM correlations in $SrTm_2O_4$ may form at higher temperatures (up to ∼250 K along the *b* axis) in agreement with the similar observation in $SrEr_2O_4$[43] and our further analysis of the D7 data (as discussed below). The measured magnetization as shown in Fig. 4(a) is strongly anisotropic, implying a potential anisotropic crystal-field effect. It is pointed out that the magnetization measured here does not need to be regularly arranged as required by a neutron diffraction study where the moment being detected has to form periodically and obey strictly the Bragg law. It is also stressed that the CW law validates only in a pure PM state as demonstrated here by our high-temperature magnetization measurements (Fig. 5).

In $SrTm_2O_4$, there exists AFM correlations and the CW temperature derived from the high-temperature measurements is -41.6(2) K. However, no evidence for a magnetic ordering, even short-ranged, appears down to ∼65 mK in our neutron-diffraction studies. This implies that there exists an extremely strong magnetic frustration for the Tm^{3+} ions in $SrTm_2O_4$ or the crystal-field energy level overwhelms that of the spin-spin interactions. As shown in Fig. 9(d), the Tm1 or Tm2 nearest-neighbour bonds (NNBs) are staggered respectively along the *c* axis, while the connections between the Tm1 or Tm2 next-NNBs (NNNBs) form ladder-like chains in the same direction. Altogether, the NNBs and NNNBs of the Tm1 or Tm2 ions form isosceles triangles for zigzag chains. These Tm chains are arranged to form bent Tm_6 honeycombs (Figs. 9(d), 9(e)). In this crystallographic environment, the similarity of the NNB and NNNB and the low coordination numbers of the Tm ions are believed to cause the geometric frustration of the spin lattice. In addition, potential stronger and competing Tm-Tm spin interactions, by virtue of the shorter NNB compared to that of the Tb-Tb ions in $SrTb_2O_4$[26], may be insufficient to overcome the crystal electric field, which therefore leads to a magnetically non-ordered state.

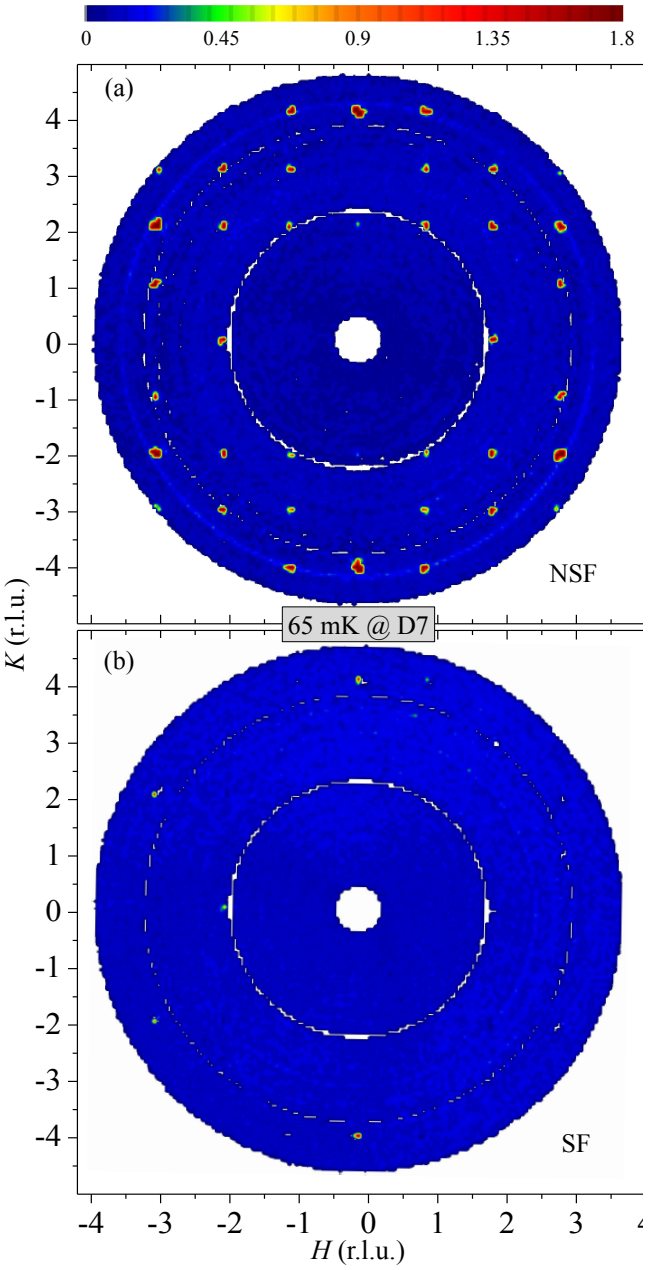

Fig. 7 Polarization analysis data measured at ∼65 mK using D7 (ILL). (a) The NSF, i.e., flipper off, and (b) SF, i.e., flipper on, channels are shown with the same colour code for intensity. The background measured at ∼1.6 K with a comparable empty sample holder was subtracted. It is pointed out that the non-perfect polarization unintentionally leads to a translucence of the strongest nuclear Bragg peaks, e.g., (0, ±4, 0), in the SF channel (details in the text).

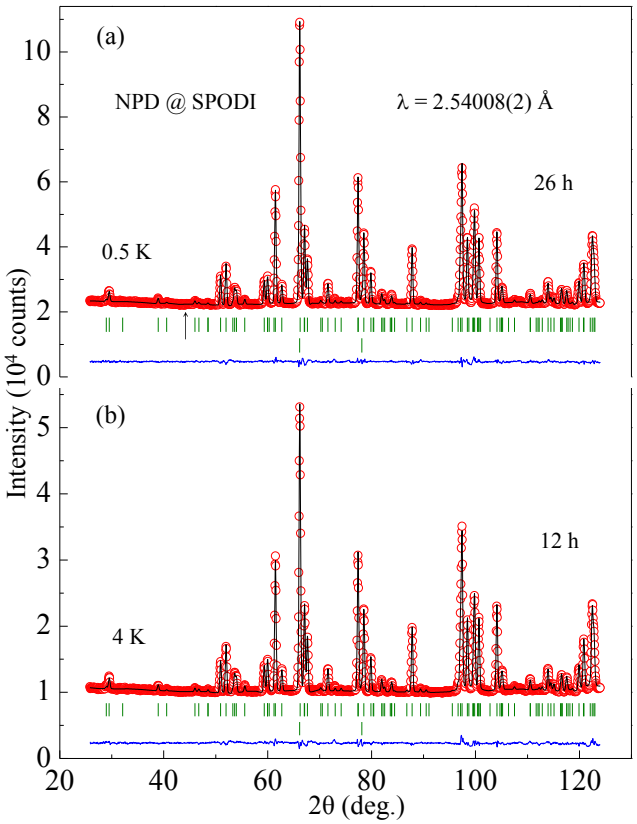

Fig. 8 Observed (circles) and calculated (solid lines) NPD patterns from the study using SPODI (FRM-II) at 0.5 K (a) and 4 K (b) with counting time ∼26 h and ∼12 h, respectively. The vertical bars in each panel mark the positions of nuclear Bragg reflections of Al (lower row) (from sample environment) and $SrTm_2O_4$ (upper row), respectively. The lower curves represent the difference between observed and calculated patterns. The vertical arrow located in (a) marks roughly the center position of the observed extremely-broad magnetic diffuse scattering which was attributed to the presence of short-ranged magnetic ordering in the polycrystalline $SrRE_2O_4$ (*RE* = Ho, Er, Dy) samples in the study of reference 21 where the wavelength employed for the NPD study is 1.5402 Å. It is clear that no appreciable diffuse magnetic scattering can be observed from the powdered $SrTm_2O_4$ single crystal.

Two explanations are possible for the refined $\eta = 0.504(1)$ at 2 K (eqn (2)). Firstly, the Tm1 and Tm2 sites present measurable magnetization, but all magnetization from both sites as a whole are nearly frustrated half even in the PM state, and the frustrated spins are in a strong freezing state. Secondly, the measurable magnetization derives from only one of the two Tm sites, probably the Tm1 site, and the magnetization from the other site (Tm2) is frustrated completely. Although both cases can lead to the slight increase in magnetization from $H_1 \sim 3.6$ to $H_2 \sim 6.5$ T as shown in Fig. 6, the later case is more favourable because it resembles the magnetic behaviour of the Tb1 and Tb2 sites in the magnetically-ordered state of $SrTb_2O_4$ [26] and is consistent with the study of $SrEr_2O_4$ [43]. Most importantly, there is no appreciable magnetic relaxation at 2 K after magnetic field has reached even 9 T. The obvious decrease in the measured magnetization above ∼8.3 T at 2 K in contrast to the theoretical Brillouin calculation (Fig. 6) may suggest a Zeeman splitting effect on the high-level *J*-multiplets.

We calculate the average octahedral distortion parameter Δ as defined by:

$$\Delta = \frac{1}{6}\sum_{n=1}^{6}\left(\frac{d_n - \langle d\rangle}{\langle d\rangle}\right)^2, \quad (8)$$

where d_n and $\langle d\rangle$ are the six Tm-O bond lengths along the six crossed directions and the mean Tm-O bond length (Table 1), respectively. We note that the Δ values of the Tm1 and Tm2 ions have a similar magnitude to that of the Tb2 ion in $SrTb_2O_4$ [26]. Since the magnetic moments associated with these three ions disorder entirely, it is thus reasonable to infer that the magnitude of the Δ value acts as an indicator of whether the RE ions in $SrRE_2O_4$ may order magnetically. In addition, as temperature decreases from 4 K to 0.5 K, the Δ value of the Tm2 ion decreases, whereas that of the Tm1 ion increases (Table 1). This reflects the temperature-dependent behavior of the Tb1 and Tb2 ions in $SrTb_2O_4$ [26]. It is necessary to explore this common tendency in other family members of $SrRE_2O_4$ compounds.

Based on the refined Tm-O bond lengths (Table 1), we deduce two distortion modes for the $Tm1O_6$ and $Tm2O_6$ octahedra as shown in Figs. 9(b) and 9(c), respectively. It is interesting that both distortion modes are the same as the corresponding ones of the $Tb1O_6$ and $Tb2O_6$ octahedra [26], indicating a common feature. Both distortion modes may be ascribed to the crystal field anisotropy, which is consistent with the computation of the crystal-field levels that demonstrate site-dependent anisotropic single-ion magnetism in the compounds $SrHo_2O_4$ and $SrDy_2O_4$ [44] and is supported by the observation in compound $SrTb_2O_4$ [26] where the partially-ordered Tb1 moments qualitatively point to the direction of the stress product imposed on the Tb1 ion by the $Tb1O_6$ octahedral distortion.

Theoretically, both Tm^{3+} and Tb^{3+} are non-Kramers ions with saturation magnetic moments of 7.0 μ_B and 9.0 μ_B, respectively. However, at 0.5 K, $SrTb_2O_4$ displays an incommensurate noncollinear AFM structure [26] with partially-ordered moments 1.92(6) μ_B (at the maximum amplitude) accommodated only at the Tb1 site. In contrast, $SrTm_2O_4$ shows no magnetic ordering. The shortest interatomic Tm-Tm (Table 1) and Tb-Tb [26] distances at 0.5 K are 3.3809 Å and 3.4523 Å, respectively, which, in conjunction with the foregoing remarks, imply that a direct exchange interaction between the

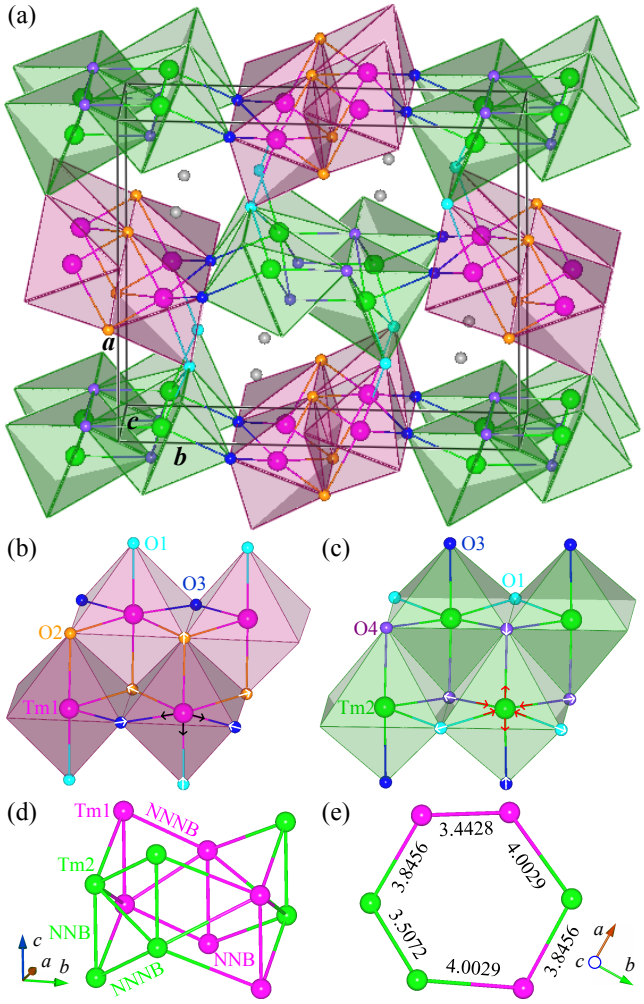

Fig. 9 (a) Crystal structure in one unit cell (solid lines) as refined from the SPODI (FRM-II) data measured at 0.5 K. Local connections and deduced distortion modes of the bent $Tm1O_6$ (b) and $Tm2O_6$ (c) octahedra. The arrows drawn through the O^{2-} ions or lying in the Tm-O bonds represent the induced stress vectors for the associated O, Tm1 and Tm2 ions (details in the text). The bent Tm_6 honeycomb (d) as well as its projection to the *ab* plane (e). In (d), the nearest-neighbour (Tm1-Tm1 = Tm2-Tm2 = 3.3809 Å) and the next-nearest-neighbour (Tm1-Tm1 = 3.4428 Å < Tm2-Tm2 = 3.5072 Å) Tm bonds are marked as NNB and NNNB, respectively.

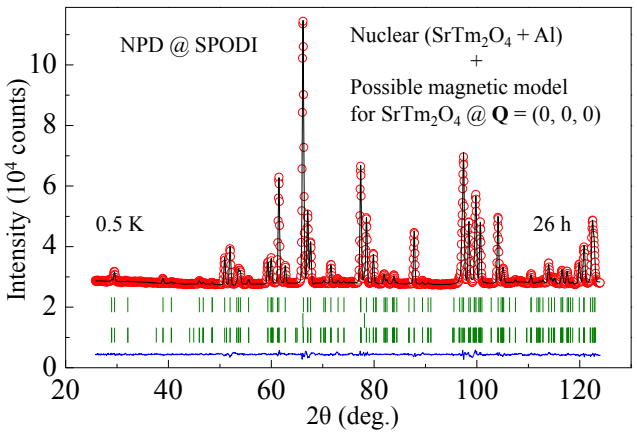

Fig. 10 (color online) Observed (circles) and calculated (solid lines) NPD patterns from the study using SPODI (FRM II) at 0.5 K with counting time ∼ 26 h. The vertical bars mark the positions of nuclear Bragg reflections of $SrTm_2O_4$ (upper row) and Al (from sample environment) (middle row), and possible magnetic Bragg peaks of $SrTm_2O_4$ with a propagation vector at **Q** = (0, 0, 0) (lower row), respectively. The lower curve represents the difference between observed and calculated patterns.

magnetic RE ions in $SrRE_2O_4$ plays no role in potential spin couplings. The implication is consistent with the fact that unpaired 4*f* electrons are well shielded by the $5s^2p^6$ shells. Although some of the ∠Tm-O-Tm bond angles (e.g., ∠Tm1-O3-Tm1 and ∠Tm1-O1-Tm2) that determine the degree of overlap of the Tm^{3+} and O^{2-} orbitals[45,46] display some temperature dependence between 0.5 K and 4 K (Table 1), the absence of magnetic ordering rules out indirect magnetic interactions through the mediator of nonmagnetic O^{2-} ions. The strong spin-orbital interaction of the RE ions may result in an anisotropic exchange, i.e., the Dzyaloshinsky-Moriya (DM) interaction, which normally requires a breaking of the inversion symmetry of the centrosymmetric $Pnam$ space group. In the study of $SrYb_2O_4$[22], forbidden nuclear Bragg peaks were indeed observed but finally were demonstrated to be entirely due to contamination from higher-order reflections. In our present studies, no such kind of forbidden peaks are observed in $SrTm_2O_4$, hence the DM interaction is unlikely to play a role in the magnetic exchange. Therefore, we conclude that the magnetic coupling in $SrTm_2O_4$ arises mainly from an anisotropic dipole-dipole interaction which, while very weak, is additionally subjected to crystal field effects resulting from the octahedral environments (as foregoing remarks).

It is interesting to compare our results with those from the corresponding pyrochlore compounds $RE_2Ti_2O_7$ (RE = Tm, Tb). In $Tm_2Ti_2O_7$, magnetic Tm^{3+} ions occupy one of the two corner-sharing tetrahedral sublattices. The crystal field effect radically dominates over the magnetic exchange interactions so that the ground state is a virtual crystal-field singlet rather than a short-ranged and frustrated magnetic state, and thus the lowest-lying crystal-field excitations do not show any appreciable dispersion[47]. In addition, the magnetic susceptibility of $Tm_2Ti_2O_7$ gets a clear plateau at low temperatures[47]. Although there exists a strong AFM interaction based on the value of the CW temperature (∼-19 K)[48], no appreciable long-range magnetic order forms in $Tb_2Ti_2O_7$ even down to 50 mK, but short-range magnetic order was indeed observed probably

indicative of a spin-liquid ground state[48,49]. The nature of the magnetic ground state and the reason for the absence of a long-range spin order in $Tb_2Ti_2O_7$ still remain elusive, which represents a theoretical puzzle and also a real experimental challenge. Our further analysis of the ω-averaged[31] neutron scattering intensity from D7 in the SF (eqn (3)) and NSF (eqn (4)) channels indeed indicates the existences of PM neutron scattering and AFM couplings in $SrTm_2O_4$ at $\sim$65 mK. However, an estimate of the moment size is complicated by the presence of strong nuclear spin-incoherent scattering. Future experiments using the XYZ polarization method at D7, which will give a clear separation between nuclear coherent, nuclear spin-incoherent and magnetic cross-sections[31], may be attempted. Our present results provide a more mysterious compound for theorists and experimentalists and also indicate that $SrTm_2O_4$ is different from other members in the family.

5 Conclusions

To summarize, we have demonstrated that there is neither long- nor short-ranged magnetic ordering in single-crystal $SrTm_2O_4$ even down to $\sim$65 mK, though the high-temperature magnetization indicates a strong net AFM coupling. The field-dependent magnetization can be fit using a modified Brillouin function for a frustrated PM state. We argue that the magnetically non-ordered state is attributed to a strong anisotropic crystal field effect. This kind of magnetic anisotropy may quench potential magnetic ordering, leading to a virtual non-magnetically-ordered state. We also find some common features for both $SrTm_2O_4$ and $SrTb_2O_4$ single crystals: (i) the measured magnetization, even in the PM state, is from just one of the two crystallographic RE sites; (ii) the same octahedral distortion modes as well as their evolutions with temperature; (iii) the spin couplings are dominated by the dipole-dipole interactions. These common features observed in both compounds may be vital to a complete understanding of the novel magnetic behaviours of $SrRE_2O_4$ compounds. Further explorations with higher magnetic fields and uniaxial pressure along the crystallographic axes, spin-density measurements in the PM state, and especially inelastic neutron-scattering studies, would be of great interest.

Acknowledgements

H.F.L acknowledges the Marie Curie-COFUND CONEX Programme by the Universidad Carlos III de Madrid, the European Commission (PCOFUNG-GA-2012-600371), the Spanish Ministry of Economy and Competitiveness (COFUND2013-40258) and Banco Santander. H.F.L is grateful to Diana Lucía Quintero Castro and Oleg Petrenko for helpful discussions and the respective sample environment teams at ILL and FRM-II for expert technical assistances.

Author contributions

H.F.L., C.Z. and G.R. grew the single crystals. J.P., B.H., J.P.V., P.T., X.S., L.W., G.K., B.S. and J.G.R. characterized the single crystal by in-house measurements. O.F. and H.F.L. performed the neutron Laue experiments and O.F. simulated the patterns. M.B., K.S., W.S. and H.F.L. performed the IN3 experiments and analyzed the data. A.S. and H.F.L. performed the SPODI experiments and analyzed the data. A.W. and H.F.L. performed the D7 experiments and analyzed the data. H.F.L., A.S., O.F., J.P., B.H., M.B., K.S., W.S., J.P.V., P.T., X.S., L.W., G.K., B.S., C.Z., G.R., J.G.R. and A.W. discussed and analyzed the results. H.F.L. and A.W. wrote the main manuscript text. A.S., O.F., K.S., G.R. and A.W. commented on the manuscript and all authors reviewed the paper. H.F.L. conceived and directed the project.

Additional information

Competing financial interests: The authors declare no competing financial interests.

References

1 H. Kawamura, *J. Phys.: Condens. Matter*, 1998, **10**, 4707.
2 A. P. Ramirez, G. P. Espinosa and A. S. Cooper, *Phys. Rev. Lett.*, 1990, **64**, 2070.
3 K. Binder, *Phys. Rev. Lett.*, 1980, **45**, 811.
4 H. T. Diep, *Frustrated Spin Systems*, World Scientific, Singapore, 2004.
5 C. Lacroix, P. Mendels and F. Mila, Introduction to Frustrated Magnetism, in *Solid-State Sciences*, Springer Series, New York, 2011, vol. 164.
6 M. J. Harris, S. T. Bramwell, D. F. McMorrow, T. Zeiske and K. W. Godfrey, *Phys. Rev. Lett.*, 1997, **79**, 2554.
7 S. T. Bramwell and M. J. P. Gingras, *Science*, 2001, **294**, 1495.
8 A. P. Ramirez, *Nature*, 2003, **421**, 483.
9 R. Moessner and A. P. Ramirez, *Physics Today*, 2006, **59**, 24.
10 Y. L. Han, Y. Shokef, A. M. Alsayed, P. Yunker, T. C. Lubensky and A. G. Yodh, *Nature*, 2008, **456**, 898.
11 D. J. P. Morris, D. A. Tennant, S. A. Grigera, B. Klemke, C. Castelnovo, R. Moessner, C. Czternasty, M. Meissner, K. C. Rule, J.-U. Hoffmann, K. Kiefer, S. Gerischer, D. Slobinsky and R. S. Perry, *Science*, 2009, **326**, 411.
12 M. J. P. Gingras, *Science*, 2009, **326**, 375.
13 S. Toth, B. Lake, K. Hradil, T. Guidi, K. C. Rule, M. B. Stone and A. T. M. N. Islam, *Phys. Rev. Lett.*, 2012, **109**, 127203.
14 Y. Xiao, Y. Su, H.-F. Li, C. M. N. Kumar, R. Mittal, J. Persson, A. Senyshyn, K. Gross and Th. Brueckel, *Phys. Rev. B*, 2010, **82**, 094437.
15 H. Djieutedjeu, X. Zhou, H. Chi, N. Haldolaarachchige, K.

G. S. Ranmohotti, C. Uher, D. Youngc and P. F. P. Poudeu, *J. Mater. Chem. C*, 2014, **2**, 6199.
16 O. A. Petrenko, *Low Temp. Phys.*, 2014, **40**, 106.
17 J.-J. Wen, W. Tian, V. O. Garlea, S. M. Koohpayeh, T. M. McQueen, H.-F. Li, J.-Q. Yan, J. A. Rodriguez-Rivera, D. Vaknin and C. L. Broholm, *Phys. Rev. B*, 2015, **91**, 054424.
18 A. A. Aczel, L. Li, V. O. Garlea, J.-Q. Yan, F. Weickert, V. S. Vapf, R. Movshovich, M. Jaime, P. J. Baker, V. Keppens, D. Mandrus, arXiv:1502.05668, 2015.
19 J. G. Pepin, *J. Appl. Cryst.*, 1981, **14**, 70.
20 T. L. Barry and R. Roy, *J. Inorg. Nucl. Chem.*, 1967, **29**, 1243.
21 H. Karunadasa, Q. Huang, B. G. Ueland, J. W. Lynn, P. Schiffer, K. A. Regan and R. J. Cava, *Phys. Rev. B*, 2005, **71**, 144414.
22 D. L. Quintero-Castro, B. Lake, M. Reehuis, A. Niazi, H. Ryll, A. T. M. N. Islam, T. Fennell, S. A. J. Kimber, B. Klemke, J. Ollivier, V. Garcia Sakai, P. P. Deen and H. Mutka, *Phys. Rev. B*, 2012, **86**, 064203.
23 B. Ouladdiaf, J. Archer, G. J. McIntyre, A. W. Hewat, D. Brau and S. York, *Physica B*, 2006, **385-386**, 1052.
24 A. A. Aczel, L. Li, V. O. Garlea, J.-Q. Yan, F. Weickert, M. Jaime, B. Maiorov, R. Movshovich, L. Civale, V. Keppens and D. Mandrus, *Phys. Rev. B*, 2014, **90**, 134403.
25 V. Lojpur, Ž. Antić and M. D. Dramićanin, *Phys. Chem. Chem. Phys.*, 2014, **16**, 25636.
26 H.-F. Li, C. Zhang, A. Senyshyn, A. Wildes, K. Schmalzl, W. Schmidt, M. Boehm, E. Ressouche, B. Hou, P. Meuffels, G. Roth and Th. Brückel, *Front. Phys.*, 2014, **2**, 42.
27 H. Li, *Synthesis of CMR manganites and ordering phenomena in complex transition metal oxides*, Forschungszentrum Jülich GmbH, Jülich, 2008.
28 H. Li, Y. Su, J. Persson, P. Meuffels, J. M. Walter, R. Skowronek and Th. Brückel, *J. Phys.: Condens. Matter*, 2007, **19**, 016003.
29 H. Li, Y. Su, J. Persson, P. Meuffels, J. M. Walter, R. Skowronek and Th. Brückel, *J. Phys.: Condens. Matter*, 2007, **19**, 176226.
30 L. Fuentes-Montero, P. Cermak and J. Rodríguez-Carvajal, unpublished (the programs of the Esmeralda Laue Suite and their documentation can be obtained from web at http://forge.ill.fr/projects/esmeralda/files).
31 J. R. Stewart, P. P. Deen, K. H. Andersen, H. Schober, J.-F. Barthélémy, J. M. Hillier, A. P. Murani, T. Hayes and B. Lindenau, *J. Appl. Cryst.*, 2009, **42**, 69.
32 M. Hoelzel, A. Senyshyn, N. Juenke, H. Boysen, W. Schmahl and H. Fuess, *Nuclear Instruments & Methods in Physics Research, Section A: Accelerators, Spectrometers, Detectors, and Associated Equipment*, 2012, **667**, 32.
33 J. Rodríguez-Carvajal, *Physica B*, 1993, **192**, 55.
34 H.-F. Li, arXiv:1404.3914, 2014.
35 H. Li, Y, Xiao, B. Schmitz, J. Persson, W. Schmidt, P. Meuffels, G. Roth and Th. Brückel, *Sci. Rep.*, 2012, **2**, 750.
36 W. Tian, J. Li, H. Li, J. W. Lynn, J. L. Zarestky and D. Vaknin, *J. Phys.: Conf. Ser.*, 2010, **251**, 012005.
37 R. Toft-Petersen, N. H. Andersen, H. Li, J. Li, W. Tian, S. L. Bud'ko, T. B. S. Jensen, C. Niedermayer, M. Laver, O. Zaharko, J. W. Lynn and D. Vaknin, *Phys. Rev. B*, 2012, **85**, 224415.
38 J. M. De Teresa, M. R. Ibarra, P. A. Algarabel, C. Ritter, C. Marquina, J. Blasco, J. García, A. del Moral and Z. Arnold, *Nature*, 1997, **386**, 256.
39 R. Mallik, E. V. Sampathkumaran, P. L. Paulose and V. Nagarajan, *Phys. Rev. B*, 1997, **55**, R8650.
40 H.-F. Li, Y. Su, Y. Xiao, J. Persson, P. Meuffels and Th. Brückel, *Eur. Phys. J. B*, 2009, **67**, 149.
41 R. S. Manna, P. Das, M. de Souza, F. Schnelle, M. Lang and J. Müller, *Phys. Rev. Lett*. 2014, **113**, 067202.
42 J. D. Zou, J. Liu and M. Yan, *J. Magn. Magn. Mater.*, 2015, **385**, 77.
43 H.-F. Li, A. Wildes, B. Hou, C. Zhang, B. Schmitz, P. Meuffels, G. Roth and Th. Brückel, *RSC Adv.*, 2014, **4**, 53602.
44 A. Fennell, V. Y. Pomjakushin, A. Uldry, B. Delley, B. Prévost, A. Désilets-Benoit, A. D. Bianchi, R. I. Bewley, B. R. Hansen, T. Klimczuk, R. J. Cava and M. Kenzelmann, *Phys. Rev. B*, 2014, **89**, 224511.
45 I. O. Troyanchuk, D. Karpinsky, V. Efimov, V. Sikolenko, O. Prokhnenko and M Bartkowiak, *J. Phys.: Condens. Matter*, 2014, **26**, 396002.
46 I. O. Troyanchuk, M. V. Bushinsky, N. V. Volkov, V. Sikolenko, E. A. Efimova and C. Ritter, *J. Exp. Theor. Phys.*, 2015, **120**, 97.
47 M. P. Zinkin, M. J. Harris, Z. Tun, R. A. Cowley and B. M. Wanklyn, *J. Phys.: Condens. Matter*, 1996, **8**, 193.
48 J. S. Gardner, *Phys. Rev. Lett*. 1999, **82**, 1012.
49 J. P. C. Ruff, Z. Islam, J. P. Clancy, K. A. Ross, H. Nojiri, Y. H. Matsuda, H. A. Dabkowska, A. D. Dabkowski and B. D. Gaulin, *Phys. Rev. Lett.*, 2010, **105**, 077203.